ADVANCED FUNCTIONAL MATERIALS
www.afm-journal.de

Rapid and Up-Scalable Flash Fabrication of Graphitic Carbon Nanocages for Robust Potassium Storage

Lina Wang, Sheng Zhu, Zhihao Huang, Mengxiu Li, Yun Zhao,* Gaoyi Han, Yan Li, and Jiangfeng Ni**

Graphitic carbon nanocages (CNCs) have garnered attention as viable candidates for potassium storage, primarily due to their notable crystallinity, large surface area, and rich porosity. Yet, the development of a rapid, scalable, and economically feasible synthesis approach for CNCs persists as a formidable challenge. This study presents a rapid (millisecond-scale) and scalable (gram-scale) method for fabricating mesoporous CNCs characterized by high purity and orderly graphitic structures, utilizing the flash Joule heating technique. Employed for potassium storage, the CNC electrode developed herein exhibits exceptional performance metrics, including initial capacity, rate capability, and cycling stability, surpassing numerous carbonaceous materials previously documented. Impressively, it delivers a high initial capacity of 312.3 mAh g^{-1} at 0.1 A g^{-1}, maintains 175.1 mAh g^{-1} at a high rate of 2.0 A g^{-1}, and retains 219.6 mAh g^{-1} over 1000 cycles at 1.0 A g^{-1}. Molecular dynamics simulations and in situ characterizations are employed to elucidate this robust behavior. This work underscores the significant advantages of the flash Joule heating technique in synthesizing carbonaceous materials for potassium storage applications.

1. Introduction

Lithium-ion batteries have seen extensive exploration across diverse fields in the past two decades, attributed to their high energy and power densities. However, the scarcity and uneven distribution of lithium reserves present obstacles to their future market development.[1–6] Recently, potassium-ion batteries (PIBs), featuring a similar "rocking chair" mechanism, have emerged as a viable alternative. The abundant reserve (2.4 wt% in the Earth's crust), low standard redox potential (2.93 V vs standard hydrogen electrode), and reduced solvation effect of potassium imbue PIBs with high operational voltage and energy density.[7,8] In the quest for high-performance potassium storage materials, graphite has been the focus due to its formation of a KC_8 intercalated compound, leading to a theoretical capacity of 279 mAh g^{-1}. However, the larger ionic radius of K ions (138 pm) compared to Li ions (76 pm) causes significant volume fluctuation and structural instability in graphite.[9] Consequently, the rational design and construction of graphitic carbon materials with robust structures are pursued to address this challenge.

Graphitic carbon nanocages (CNCs), a kind of cage-like carbon nanomaterials composed of curved graphite nanosheets, have attracted considerable scientific interest due to their high crystallinity, large surface area, and rich porosity.[10] In recent years, CNCs, with their distinctive hollow internal structure, have gained increasing recognition in potassium storage as their pores can accommodate volume variations.[11,12] Naturally, the efficient synthesis of highly crystalline CNCs is a prerequisite for their widespread application in PIBs. Typically, CNCs have been fabricated through high-temperature graphitization or catalytic synthesis. For instance, Song et al.[13] produced CNCs by annealing Ketjen carbon black at 2800 °C, resulting in impressive rate capability and cycling stability. However, high temperatures and energy consumption pose challenges for their practical prospect. To reduce the synthesis temperature (<1200 °C), a catalytic synthesis using transition metal catalysts (e.g., Fe, Co, and Ni) has been developed.[14–16] Nevertheless, the complete removal of metal catalysts is challenging due to the high acid oxidation resistance of the graphite shells, and this process inevitably damages the graphitic structure of CNCs, leading to poor

L. Wang, S. Zhu, Y. Zhao, G. Han
Institute of Molecular Science
Key Laboratory of Materials for Energy Conversion and Storage of Shanxi Province
Key Laboratory of Chemical Biology and Molecular Engineering of Education Ministry
Shanxi University
Taiyuan 030006, China
E-mail: shengzhu@sxu.edu.cn; yunzhao@sxu.edu.cn

S. Zhu, G. Han, Y. Li
Institute for Carbon-Based Thin Film Electronics
Peking University
Shanxi (ICTFE-PKU)
Taiyuan 030012, China

Z. Huang, M. Li, J. Ni
School of Physical Science and Technology
Center for Energy Conversion Materials & Physics (CECMP)
Jiangsu Key Laboratory of Thin Films
Jiangsu Key Laboratory of Advanced Negative Carbon Technologies
Soochow University
Suzhou 215006, China
E-mail: jeffni@suda.edu.cn

The ORCID identification number(s) for the author(s) of this article can be found under https://doi.org/10.1002/adfm.202401548

DOI: 10.1002/adfm.202401548

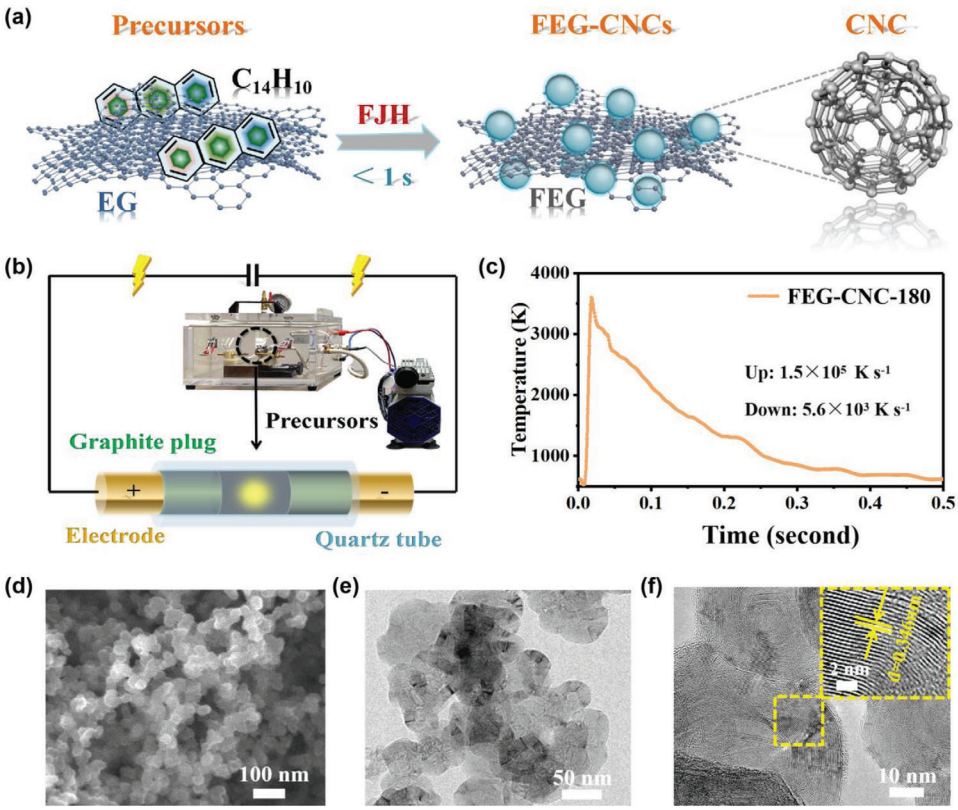

Figure 1. Synthesis and morphology of FEG-CNCs. a) Schematic illustration of the preparation process of FEG-CNCs. b) Schematic of the FJH equipment. c) Plot of the temperature versus time for FEG-CNC-180 during the FJH process. d) SEM, e) TEM, and f) HRTEM images of FEG-CNC-180.

electrochemical performance.[17–19] Thus, developing a simple, scalable, and catalyst-free approach to produce CNCs with high purity and quality is crucial.

In this study, we report the ultrafast and efficient synthesis of CNCs through a flash Joule heating (FJH) technique within hundreds of milliseconds. The FJH method eschews metal-containing catalysts, chemical solvents, or special gas atmospheres, generating high instantaneous temperatures exceeding 3000 K, which facilitate the formation of highly graphitic and cage-like carbon materials. As-synthesized CNCs demonstrate superior potassium storage performances, including high reversible capacity, ultrastable long-term cyclability, and excellent rate capacity. Molecular dynamics simulations indicate that CNCs with a curved structure exhibit much lower K^+ adsorption energy compared to planar graphite. Moreover, the potassium storage mechanism of CNCs has been investigated through both in situ Raman and ex situ XRD measurements. This study contributes valuable insights into the rational construction and structure modulation of CNCs for advanced energy storage, leveraging the FJH technique.

2. Results and Discussion

Figure 1a schematically depicts the utilization of conductive expanded graphite (EG) as substrate for the synthesis of CNCs. In this process, the precursor, polycyclic anthracene ($C_{14}H_{10}$), undergoes pyrolysis, forming CNCs during the flash Joule heating procedure. The resultant material is designated as FEG-CNCs. On the one hand, $C_{14}H_{10}$ molecules are composed of sp^2 carbon atoms, which tend to form highly graphitic carbon materials at high temperature. On another hand, the ultrahigh heating/cooling rates and uneven molecule evaporation during instantaneously high temperature would lead to the generation of hollow CNCs.[20–22] Given the propensity of $C_{14}H_{10}$ to volatilize at temperatures exceeding 340 °C, a preliminary heating treatment was employed to securely anchor the $C_{14}H_{10}$ molecules onto the graphite surface. This step was executed in a muffle furnace at 300 °C. Scanning electron microscopy (SEM) images presented in Figure S1 (Supporting Information) display the EG@$C_{14}H_{10}$ post-treatment, where a discernible layer of crystalline $C_{14}H_{10}$ is evident on the EG surface. The precursor is then exposed to an exceptionally high temperature exceeding 3000 K in less than one second through FJH method, as evidenced by the intense luminescence observed (Video S1, Supporting Information). Figure 1b illustrates a typical FJH reaction system, comprising three principal components: electrode rods, a quartz tube, and graphite plugs. To initiate the FJH reaction, the precursors are gently compressed within a quartz tube, flanked by two graphite plugs, allowing for the modulation of sample resistance by altering the distance between the plugs. The high-voltage electric discharge generates a transient peak temperature of ≈3600 K, with a heating rate of $\approx 1.5 \times 10^5$ K s^{-1}. The cooling rate post heating is estimated to be $\approx 5.6 \times 10^3$ K s^{-1}, as illustrated in Figure 1c. Optical photographs of the FJH reactor, both prior to and during

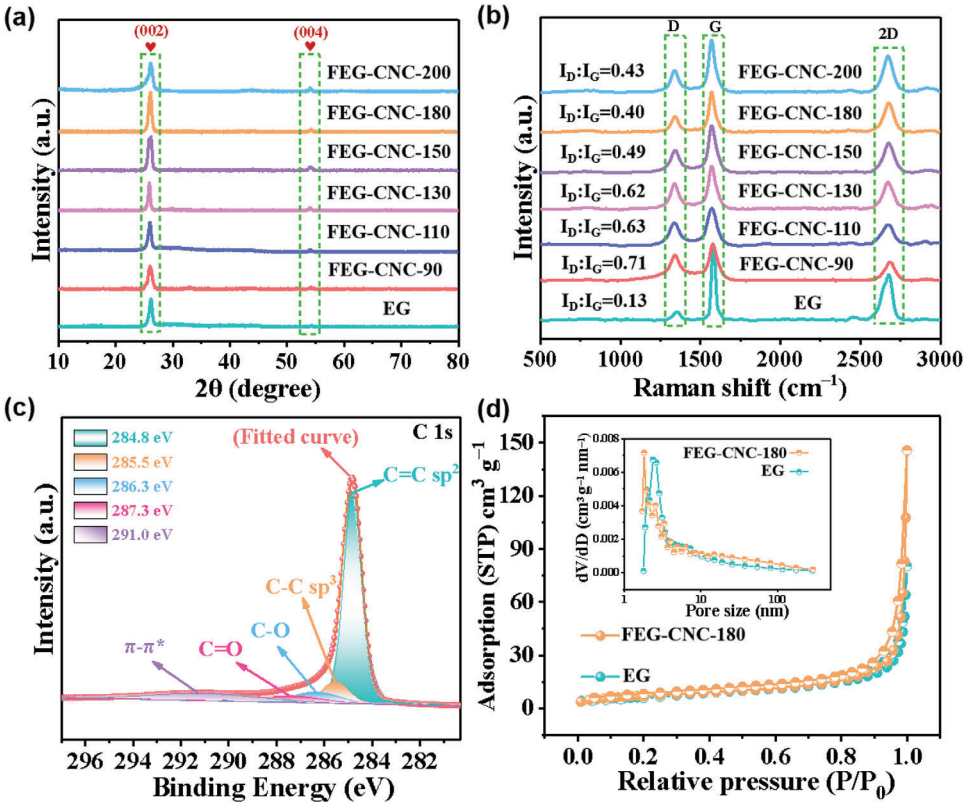

Figure 2. Characterization of FEG-CNCs at different flash voltages. a) XRD patterns and b) Raman spectra of FEG-CNCs under different flash voltage and EG samples. c) High-resolution C 1s XPS spectrum of FEG-CNC-180. d) N_2 adsorption/desorption curves and pore size distributions of FEG-CNC-180 and EG samples.

the reaction, are presented in Figure S2 (Supporting Information). Following the FJH process, the initially gray EG@$C_{14}H_{10}$ precursor transforms to the black FEG-CNCs (Figure S3, Supporting Information).

The morphological characteristics of the fabricated FEG-CNC samples were controlled by modulating the flash voltages, which are intricately linked with the resultant reaction temperatures.[23] This relationship is exemplified in Figure S4 (Supporting Information), where the temperatures corresponding to flash voltages of 90, 110, 130, 150, 180, and 200 V were determined to be 1997, 2130, 2585, 2991, 3616, and 3878 K, respectively. Detailed flash parameters can be found in (Table S1, Supporting Information). Analysis of SEM images (Figure 1d; Figure S5 and S6, Supporting Information) reveals that the CNC-180 sample exhibits the most regular and uniform spherical morphology, with an average outer diameter of ≈50 nm. The cage-like architecture of the flash products was further elucidated through transmission electron microscopy (TEM) and high-resolution TEM (HRTEM). Figure 1e,f highlights the FEG-CNC-180 sample, showcasing distinct lattice fringes with a d-spacing of 0.346 nm (inset in Figure 1f), indicative of a graphitic structure.[24] These dense carbon nanocages are primarily composed of multiple graphene layers with a wall thickness of 10–20 nm. Furthermore, the influence of the FJH method on the EG substrate was investigated. As depicted in Figure S6 (Supporting Information), the FEG substrate retains its layered configuration without significant structural damage, attributable to the extremely short duration (<1 s) of the FJH process. In stark contrast, prolonging the pulse duration to 60 s at 3000 K leads to substantial agglomeration of the EG layers, as evident in Figure S7 (Supporting Information). The collective analysis suggests that the FJH technique facilitates the thermal decomposition of anthracene into FEG-CNCs without damaging the structural integrity of the EG matrix.

The XRD pattern of the EG@$C_{14}H_{10}$ precursor reveals a coexistence of EG and polycyclic anthracene phases (Figure S8, Supporting Information), which remains undecomposed at lower temperatures. **Figure** 2a presents the XRD patterns of FEG-CNCs produced at varying flash voltages. The observed characteristic peaks correspond exclusively to the (002) and (004) crystal planes of graphite, with no detectable impurities. Notably, as the flash voltage increases from 90 to 180 V, there is a discernible enhancement in the intensity of the (002) diffraction peak, indicative of improved graphitization. However, an anomalous trend is noted at a higher voltage of 200 V. Raman spectroscopy further elucidates their structural characteristics, as displayed in Figure 2b. The D-band (≈1340 cm^{-1}) is indicative of structural defects or stacking disorders, while the G-band (≈1570 cm^{-1}) represents the E_{2g} vibration mode of sp^2 hybridized carbon.[25,26] The intensity ratio of the D-band to G-band (I_D/I_G) is a conventional metric for assessing the degree of graphitization in carbon materials. A declining trend in I_D/I_G ratios is observed with increasing flash voltages from 90 to 180 V. The FEG-CNC-180 sample exhibits the lowest I_D/I_G ratio of ≈0.40 and the highest I_{2D}/I_G ratio of ≈1.83, suggesting a more crystalline structure.[27] This

observation is consistent with the XRD results. Importantly, no significant alterations of EG occur before and after the FJH process despite the transient high-temperature exposure (Figures S9, Supporting Information). Figure S10 (Supporting Information) shows the infrared spectra of products collected at different flash voltages. Thermogravimetric analysis reveals that EG undergoes decomposition near 500 °C, whereas the FEG-CNC-180 sample maintains stability up to approximately 600 °C (Figure S11, Supporting Information). This finding underscores the excellent thermal stability of the FEG-CNC-180 sample following FJH treatment.

X-ray photoelectron spectroscopy (XPS) was employed to analyze the surface chemical composition of the FEG-CNC-180 and EG samples, as depicted in Figures S12–S14 (Supporting Information). These spectra confirm the presence of both C and O elements in both samples. Notably, the FEG-CNC-180 sample exhibits a higher C/O atomic ratio compared to EG. This observation suggests a more carbon-rich composition in the FEG-CNC-180 sample. High-resolution C 1s spectra reveal major peaks at ≈284.8 and 285.5 eV, which are attributed to sp^2 hybridized graphitic carbon and sp^3 hybridized amorphous carbon, respectively (Figure 2c). The presence of weak C—O and C═O groups, evidenced by binding energies ≈286.3 and 287.3 eV for both samples, is likely a consequence of minor oxidation of the carbon material by atmospheric oxygen.[28,29] Furthermore, the different chemical states of oxygen in the samples are elucidated by two distinct peaks in the O1s spectra, located at 532.7 and 534.6 eV, corresponding to C—O and C═O bonds, respectively.[30,31] In addition, nitrogen adsorption–desorption isotherms were conducted to determine the surface area of the materials. As shown in Figure 2d, FEG-CNC-180 demonstrates a BET surface area of 34.45 $m^2 g^{-1}$, which is significantly larger than that of EG (23.67 $m^2 g^{-1}$). The larger surface area in FEG-CNC suggests a higher availability of active sites for K^+ storage.[32]

The physical and chemical attributes of FEG-CNC-180 render it a prime candidate for use as an anode material in PIBs. The representative CV curves of the FEG-CNC-180 electrode, conducted at a scan rate of 0.25 mV s^{-1} in a 2025-type coin half-cell with 0.8 M KPF_6 in EC:DEC (1:1 v/v) electrolyte, are shown in **Figure** 3a. During the initial cathodic sweep, a pronounced peak at 0.01 V is observed, indicative of K^+ insertion into the graphite layers of the material. Additionally, a broad reduction peak spanning a potential range of 0.2–1.1 V is evident only in the first cycle, which might be attributed to the formation of a solid electrolyte interface (SEI).[33,34] In the anodic scan, a significant peak at approximately 0.3 V corresponds to the deintercalation of K^+ from the graphite layers.[35] Subsequent CV cycles exhibit well-overlapping curves, suggesting high reversibility in the electrochemical cycling process. Notably, the CV profile of FEG-CNC-180 closely resembles that of EG (Figure S15, Supporting Information), indicating a similar K-ion storage mechanism. Figure 3b shows the charge–discharge profiles of FEG-CNC-180 across various cycles at a current density of 0.1 A g^{-1}, which reflects similar electrochemical behaviors to that of CV analyses. In the first discharge, an irreversible and gentle slope in the range of 0.2–1.0 V can be observed, which disappears in the following cycles, corresponding to the formation of the SEI film. In the low-voltage region of the discharge curve, the plateau appearing at ≈0.1 V are related to the intercalation reaction of K^+. In the subsequent discharge curves, another new voltage plateau at ≈0.25 V is associated with K^+ insertion and the formation of a series of graphite intercalation compounds from KC_{36} to KC_8. The long charge plateau at around 0.3 V can be observed during the entire charge process, which corresponds to the deintercalation of K^+ from graphite layers. It also demonstrates a reversible capacity of 312.3 mAh g^{-1} in the first cycle, superior to EG (Figure S16, Supporting Information). However, the electrode receives an initial Coulombic efficiency (ICE) of 42.2%. As far as we know, the side reactions between electrode and electrolyte and the formation of unstable SEI would lead to low ICE and large irreversible capacity. These problems could be ameliorated using the strategies of prepotassiation, electrolyte optimization, and/or heteroatom doping, thus promoting its future application.[36–40] Remarkably, a stable capacity in subsequent cycles is evident, highlighting its structural stability. For further assessment, GCD tests were conducted over 100 cycles in coin half-cells. As illustrated in Figure 3c, FEG-CNC-180 delivers a reversible capacity of 298.7 mAh g^{-1} after 100 cycles, with a CE of ≈100% and a capacity retention of 95.6%. In comparison, EG only exhibits a capacity of 187.9 mAh g^{-1} and a capacity retention of 76.5%, further underscoring the superiority of FEG-CNC-180. Electrolytes play a key role in the electrochemical performance of energy storage systems.[41–43] Based on this, we further assessed the electrochemical performance of the FEG-CNC-180 electrode using another electrolyte (0.8 M KPF_6 EC:EMC (1:1 v/v)). However, it presented poorer stability than the used electrolyte of 0.8 M KPF_6 EC:DEC (1:1 v/v) (Figure S17, Supporting Information). In addition, potassium storage behavior of FEG-CNC-180 as a cathode material was also been evaluated, as shown in Figure S18 (Supporting Information).

Figures 3d and S19 (Supporting Information) compare the rate capability of FEG-CNC-180 with EG under varying current densities. At current densities of 0.1, 0.25, 0.5, 0.75, and 1.0 A g^{-1}, the FEG-CNC-180 electrode achieves capacities of 309.8, 278.3, 244.2, 224.8, and 206.8 mAh g^{-1}, respectively, which are consistently greater than those of EG. Even at a high rate of 2.0 A g^{-1}, the FEG-CNC-180 maintains a capacity of 175.1 mAh g^{-1}, corresponding to a capacity retention of 56.5%. In contrast, EG retains only 8.4% of its initial capacity at the same current density. It is believed that the unique structural design of FEG-CNC-180, featuring graphitic carbon layers and 3D interconnected cage-like structure, plays a pivotal role in its robust electrochemical performance (Figure 3e).[44] This structure allows for rapid electron transport between adjacent carbon nanocages and shortens the ion diffusion path within the solid phase.[11,13,45] However, the open layered structure of planar EG cannot withstand large interlayer changes during K^+ intercalation/deintercalation, resulting in structural degradation. It is noted that the rate performance of FEG-CNC-180 is superior to many reported CNC and carbon-based anodes, as detailed in Figure 3f and Table S2 (Supporting Information).[16,46–51] We highlight the long-term stability and cycling efficiency of the flash CNC material in Figure 3g. After 1000 cycles, the FEG-CNC-180 electrode consistently maintains a high reversible capacity of 219.6 mAh g^{-1}, with a CE nearing 100%. Additionally, the electrochemical behaviors of FEG-CNC anodes prepared at various flash voltages are assessed (Figure S20, Supporting Information). It is evident from this analysis that the FEG-CNC-180 electrode outperforms others in terms

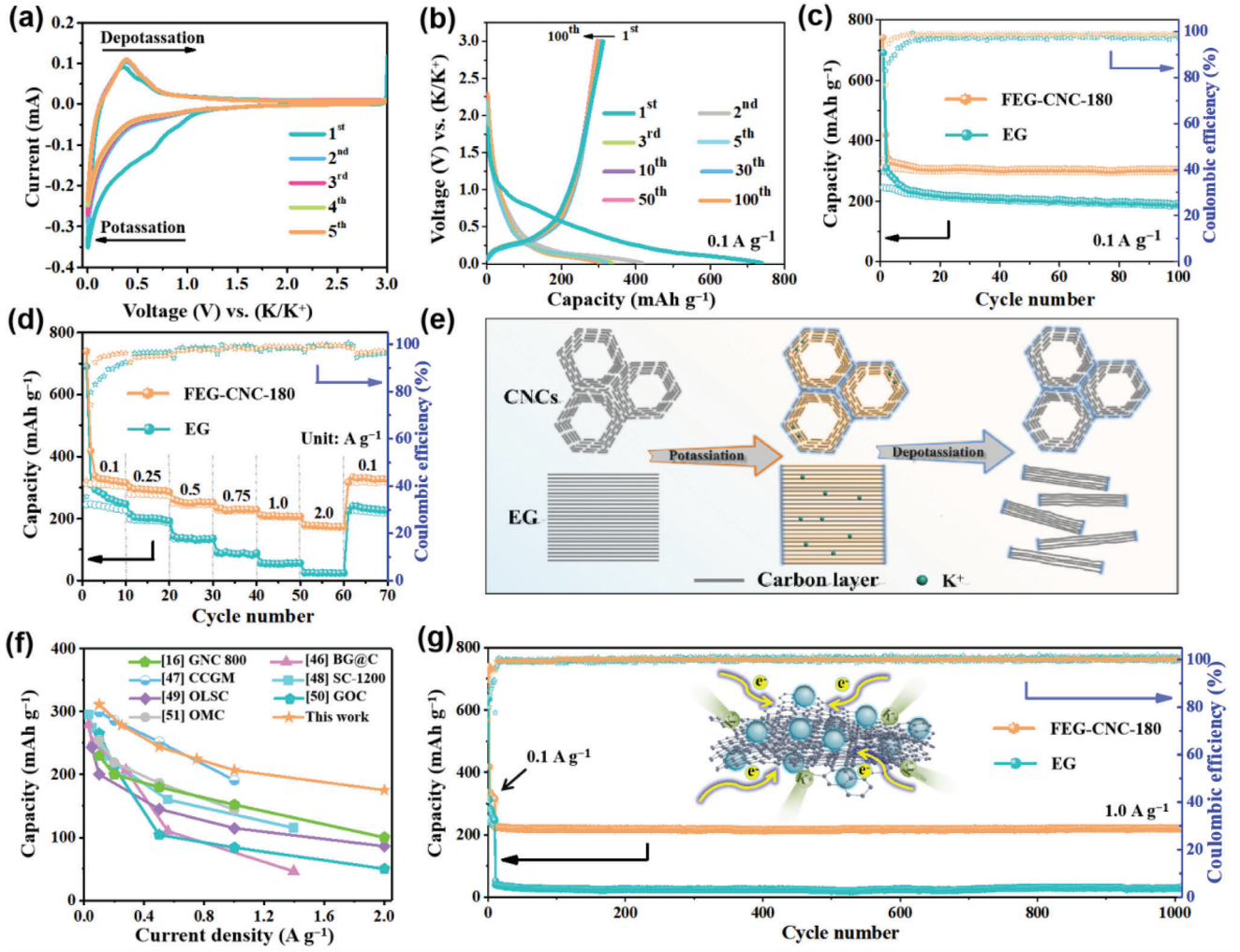

Figure 3. Potassium storage performance. a) CV curves at a scan rate of 0.25 mV s^{-1} and b) discharge/charge voltage profile at 0.1 A g^{-1} of FEG-CNC-180. c) Cycling performance at 0.1 A g^{-1} of FEG-CNC-180 and EG. d) Rate capacity at various current densities from 0.1 to 2.0 A g^{-1} of FEG-CNC-180 and EG. e) Schematic illustration of structural variations of FEG-CNC-180 and EG electrodes during potassiation and depotassiation. f) Comparison of the rate capability of the FEG-CNC-180 anode with reported other carbonaceous anodes for PIBs. g) Comparison of long-term cycle stability at 1.0 A g^{-1} of FEG-CNC-180 and EG.

of reversibility and rate capability during potassiation and depotassiation. SEM and TEM imaging of the FEG-CNC-180 electrode after 100 cycles were conducted and presented in Figure S21 (Supporting Information). These images reveal that the electrode maintains its original morphology and the interconnected cage structure remains intact. Specifically, we carried out the controlled experiments without EG substrate. As shown in Figure S22 (Supporting Information), the prepared carbon nanocages also deliver a desirable capacity of 274.5 mAh g^{-1} after 100 cycles with a capacity retention of 97.1% at 0.1 A g^{-1}. Importantly, the electrochemical properties of FEG also remain unchanged after undergoing the FJH process (Figure S23, Supporting Information).[52,53] Those results further validate that carbon nanocages mainly contribute to the robust potassium storage performance of FEG-CNC-180.

To elucidate the K^+ storage mechanism, XRD analyses of FEG-CNC-180 were performed during the initial discharge–charge cycle. Throughout the process, the formation of various potassium intercalation compounds (KC_x) is observed, aligning with previous findings.[54] During the discharge (points *a* to *f*), the intensity of the (002) graphite peak at 26.4° progressively diminishes, while new diffraction peaks corresponding to KC_{36} (22.03°/29.51°), KC_{24} (20.35°/30.72°), and KC_8 (16.48°/33.46°) appear. In the subsequent charge process, the peaks due to the KC_x phases gradually weaken and finally vanish at the cut-off voltage of 3 V (point *i*).[55,56] Such a peak evolution confirms the highly reversible and step-wise transitions of KC_{36}, KC_{24}, and KC_8 during the potassiation and de-potassiation processes, as visualized in **Figures** 4a,b and S24 and S25 (Supporting Information).[57] In addition, in situ Raman spectroscopy was further utilized to probe the structural changes of FEG-CNC-180 induced by K^+ intercalation. Figure 4c illustrates that the intensity of the D and G bands decreases as the electrode is discharged to 0.01 V, correlating with the migration of K ions into the carbon layers, forming staged intercalation compounds.[58] Notably, a red shift in the G peak during prolonged discharge is observed, likely

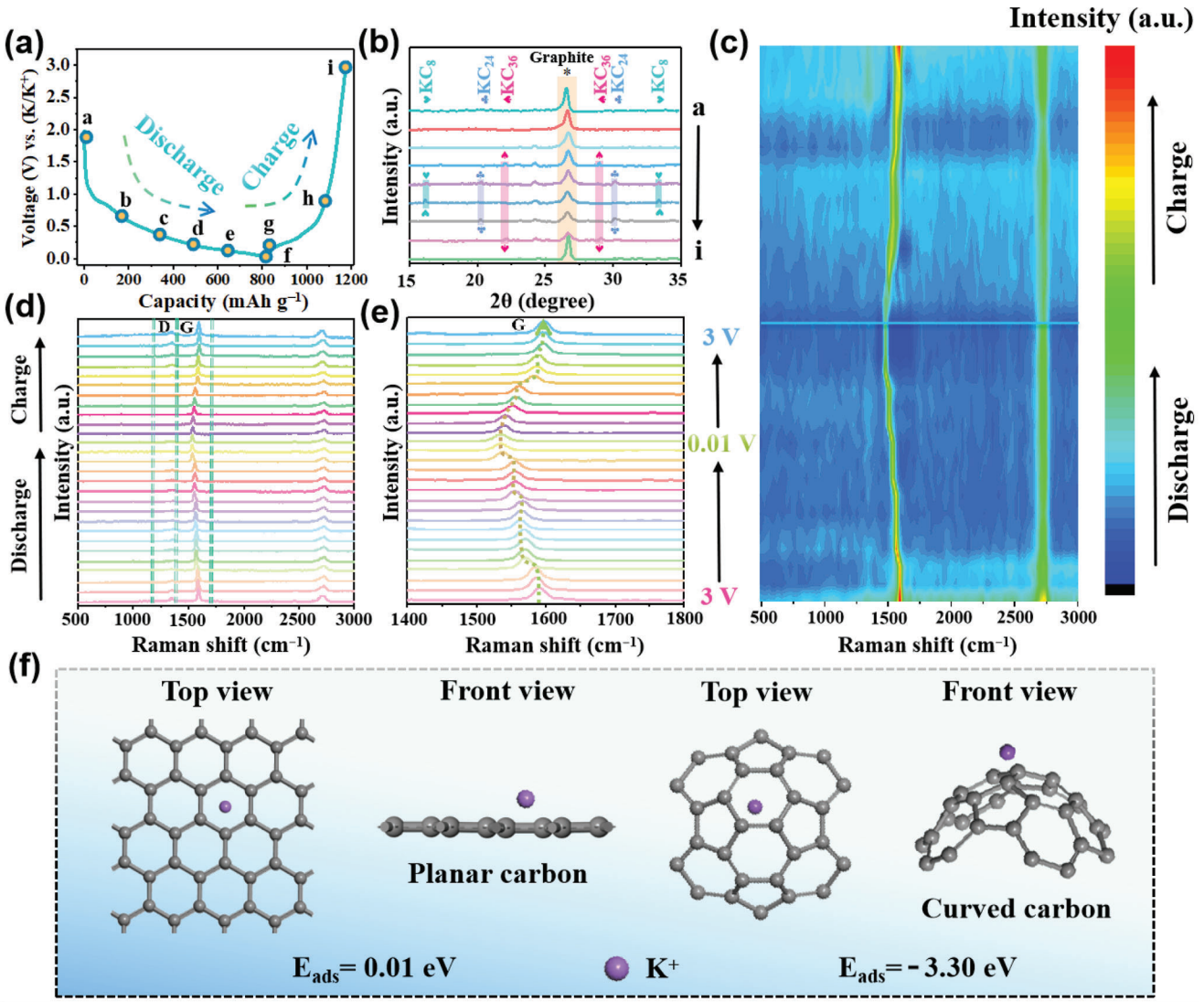

Figure 4. Structural evolution. a) Galvanostatic charge–discharge profile and b) corresponding ex situ XRD patterns at various voltage states during the initial discharge–charge cycle. c) In situ Raman spectra and d) detailed variation of the G peaks upon potassiation and depotassiation process. e) The contour plot of all Raman spectra during the in situ Raman experiment. f) The molecular dynamics simulations models with top- and front-view of K^+ absorbing on planar and curved carbon surfaces.

due to the stretching of the in-plane C–C bond resulting from increased electron density and steric hindrance following K^+ insertion, as shown in Figure 4d. Upon recharging to 3 V, the G peak intensity returns to its original state, corroborating the high reversibility of the FEG-CNC-180 anode, consistent with observations in Figure 4e.[35,59] Furthermore, molecular dynamics simulations were conducted using the Forcite module in the Materials Studio 2022 software. The simulations, detailed in Figure 4f, reveal that the adsorption energy (E_{ads}) of K^+ on curved graphite surfaces is −3.30 eV, significantly lower than 0.01 eV for planar graphitic carbon. This suggests that CNCs with curved graphite structures are more favorable for K^+ adsorption and storage, thereby enhancing their effectiveness as anode materials.[60,61]

CV curves of FEG-CNC-180 in **Figure 5a** display consistent shapes across various scan rates. The slight shifts in peak positions at higher scan rates indicate minimal polarization and excellent electrical conductivity, ideal for electrochemical applications.[62,63] The relationship between the peak current (i) and the scan rate (v) is quantitatively described by the following equations:[64]

$$i = av^b \quad (1)$$

$$\log i = b \log v + \log a \quad (2)$$

where Equation 1 is the power-law relation and Equation 2 is its logarithmic form. The constants a and b can be determined from the slope of the log (i) versus the log (v) plot. The value of b is indicative of the charge storage mechanism: values close to 1 suggest capacitive-dominated behavior, while those approaching 0.5 are characteristic of Faradaic intercalation processes. FEG-CNC-180 reveals b-values of 0.765 and 0.815 for oxidation

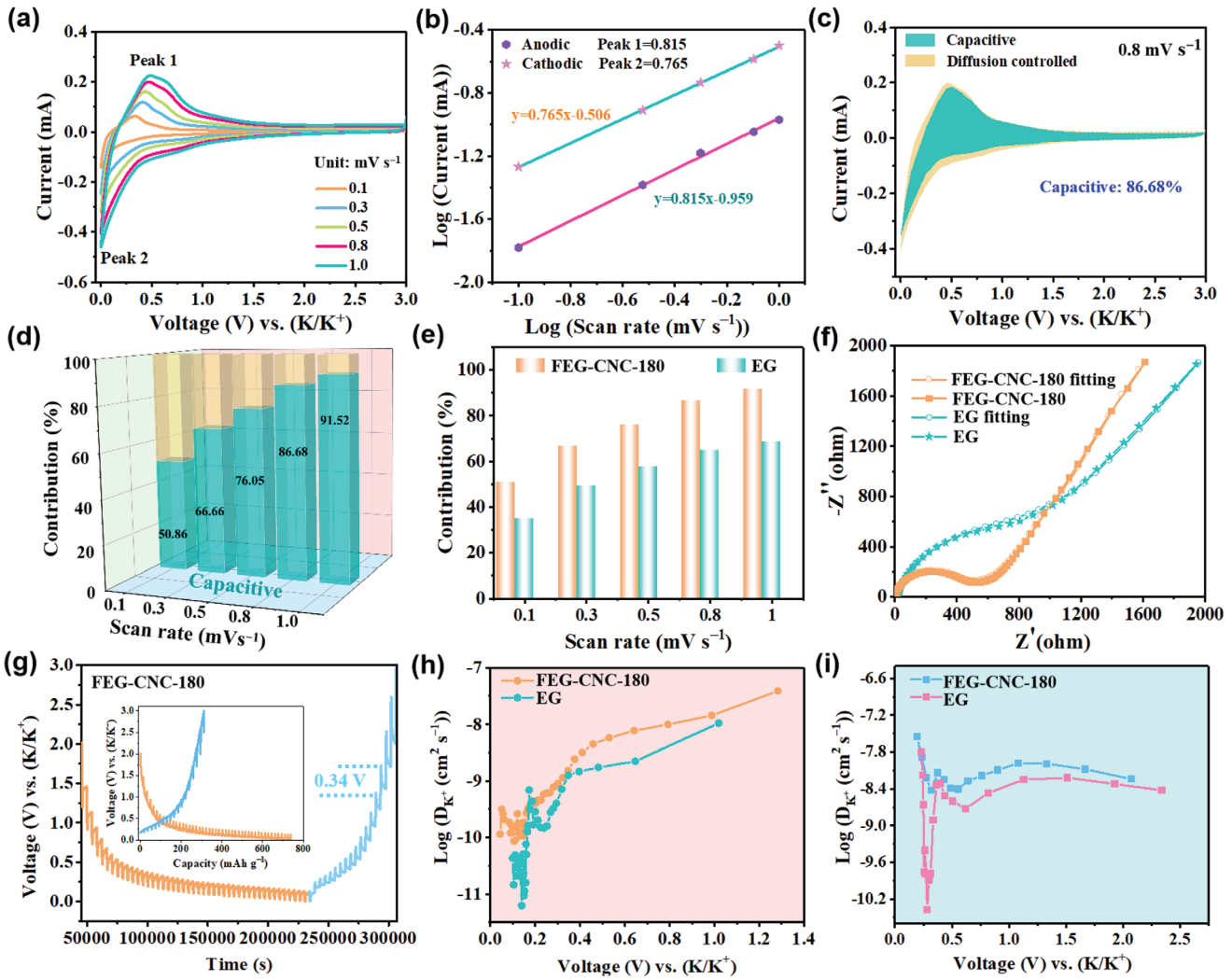

Figure 5. Kinetics analyses of FEG-CNC-180. a) CV curves of FEG-CNC-180 with scan rates ranging from 0.1 to 1.0 mV s^{-1}. b) *b*-values of anodic and cathodic peaks of FEG-CNC-180. c) Pseudocapacitive contribution (dark cyan region) at a scan rate of 0.8 mV s^{-1}. d) The contribution of the capacitance in the FEG-CNC-180 at different scan rates. e) Contribution of capacitance control contributions of FEG-CNC-180 and EG electrodes at different scan rates. f) Impedance comparison after 10 cycles of CNCs 180 and EG. g) The GITT curves and GITT voltage profiles (inset in Figure 5g) of FEG-CNC-180 during the first cycle. D_{K^+} calculated from the first h) discharge and i) charge GITT curves for FEG-CNC-180 and EG electrodes during the first cycle at 0.1 A g^{-1}.

and reduction, respectively, implying a predominantly pseudocapacitive K^+ storage. (Figure 5b). This implies that surface reactions contribute significantly to charge storage, which is advantageous for high-rate performance. The capacitive and diffusion-controlled contributions are further differentiated using the equations:[65]

$$i(V) = k_1 v + k_2 v^{1/2} \quad (3)$$

$$i/v^{1/2} = k_1 v^{1/2} + k_2 \quad (4)$$

where $k_1 v$ represents the capacitive process and $k_2 v^{1/2}$ is the diffusion-controlled process. As depicted in Figures 5c and S26 (Supporting Information), the capacitive charge proportion of the FEG-CNC-180 anode at a scan rate of 0.8 mV s^{-1} is 86.68%, substantially higher than the 64.71% observed for the EG anode. This indicates that the FEG-CNC-180 has superior charge-transfer kinetics.[66] Additionally, the pseudocapacitive contributions are estimated to be 50.86%, 66.66%, 76.05%, 86.68%, and 91.52% at the scan rates of 0.1, 0.3, 0.5, 0.8, and 1.0 mV s^{-1}, respectively, revealing that the capacitive contribution improves gradually along with the increase of the scanning rates (Figure 5d). Moreover, at each scan rate, the FEG-CNC-180 exhibits higher capacitive contributions compared to the EG anode, as shown in Figure 5e. This high capacitive contribution is likely due to the unique conductive network formed by the highly graphitic CNCs with curved structures. This feature not only enhances the electrode stability but also improves its overall conductivity, facilitating rapid K-ion storage.[67,68] The electrochemical impedance spectra (EIS) in Figure 5f reveal that the FEG-CNC-180 demonstrates a reduced semicircle diameter and a more pronounced linear slope in comparison to EG, suggesting the enhanced kinetics for K^+

intercalation and deintercalation in the CNC-intermingled graphitic electrode material.[69,70]

The galvanostatic intermittent titration technique (GITT) was employed to characterize the FEG-CNC-180 during its initial cycle. Figure 5g illustrates these GITT curves, aligning with the standard galvanostatic charge–discharge profiles at a current density of 0.1 A g^{-1}. An expanded view of the potential response during a singular current pulse is presented in Figure S27 (Supporting Information), where τ denotes the relaxation time, ΔE_s represents the steady-state potential change, and ΔE_t signifies the comprehensive potential change during the constant current pulse, post iR- drop correction.[71] Notably, FEG-CNC-180 demonstrates diminished potential fluctuations (0.34 V) compared to EG (0.45 V), as depicted in Figure S28 (Supporting Information). This indicates a lower overpotential and expedited reaction kinetics for the former. The K^+ diffusion coefficients (D_{K^+}) across varying discharge/charge potentials are calculated utilizing Equation 5:

$$D_{K^+} = \frac{4}{\pi\tau}\left(\frac{mV_m}{MS}\right)^2\left(\frac{\Delta E_s}{\Delta E_t}\right)^2 \quad (5)$$

where m, V_m, M, and S denote the active mass (g), molar volume (cm^3 mol^{-1}), molar mass (g mol^{-1}), and electrode surface area (cm^2), respectively.[72,73] Figure 5h,i illustrate that the K^+ diffusion coefficients in the FEG-CNCs electrode consistently surpass those in EG across nearly all voltages during the potassium ion insertion/extraction processes. This underscores that the FEG-CNC-180 electrode exhibits superior ion diffusion kinetics.[74]

3. Conclusion

In conclusion, we have demonstrated a rapid and scalable synthesis of CNCs via an FJH method. The resulting CNCs, characterized by high crystallinity and large surface area, are promising candidates as anode materials for PIBs. Notably, the optimized FEG-CNC demonstrates a substantial initial capacity of 312.3 mAh g^{-1} at a current density of 0.1 A g^{-1}, maintaining over 95.6% capacity after 100 cycles. Moreover, it exhibits a capacity of 175.1 mAh g^{-1} at a higher current density of 2.0 A g^{-1}, which notably surpasses that of traditional graphite anodes. The structural evolution of the CNC electrode during discharge and charge has been meticulously analyzed using in situ Raman spectroscopy and ex situ XRD techniques. These analyses have revealed the high reversibility of the phase transitions in potassium interaction compounds. Furthermore, molecular dynamics simulations have corroborated that CNCs, with their curved graphite structure, are more conducive for potassium adsorption and storage. Collectively, these findings highlight the great potential of FJH in the development of advanced carbon-based materials for energy storage applications.

4. Experimental Section

Synthesis of the EG@$C_{14}H_{10}$ Precursor: Commercial anthracene (98%) was purchased from Shanghai Macklin Biochemical Co., Ltd. Expanded graphite (99.5%, 80 mesh) was synthesized according to the prior research as a conductive additive.[75] To realize a uniform deposition of $C_{14}H_{10}$ on the surface of EG, first, EG and $C_{14}H_{10}$ were blended in an agate mortar at a mass ratio of 1:30 for 5 min. Subsequently, the mixture was transferred into an Ar-protected stainless steel autoclave with a volume of 100 mL and raised the temperature to 300 °C for 2 h at a heating rate of 5 °C min^{-1}. Then, the EG@$C_{14}H_{10}$ precursor was obtained.

Synthesis of the FEG-CNCs: The FEG-CNCs were fabricated through a facile FJH route with the EG@$C_{14}H_{10}$ as the precursor. Detailly, the EG@$C_{14}H_{10}$ precursor was encapsulated into a quartz tube with a size of Φ11 mm × 70 mm. A graphite plug was placed at one end, followed by adding 100 mg of the precursor material in the middle and another graphite plug at the opposite end, forming a relatively closed contact between the precusor sample and the plugs. The plugs at the end of the quartz tube were connected to two conductive copper electrodes and suspended on a tube holder. The FJH reaction was conducted in a vacuum box, where alternating current was converted into direct current using a switch power supply to charge the capacitors. The power stored in the capacitors was released instantaneously by heating the FEG@$C_{14}H_{10}$ precursor to extremely high temperatures (exceeding 3000 K in some cases) in less than one second, followed by rapid cooling back to ambient temperature. According to Ohm's law, the resistance of the feedstock influences the intensity of current discharge, thus controlling the generated heat. In this scenario, twice predischarge treatments were performed by using a 30 V flash voltage to lower the initial resistance within 2 Ω. Then, the FJH experiments were carried out by employing different voltages (i.e., 90, 110, 130, 150, 180, and 200 V) to vary the pulse current. The corresponding samples were denoted as FEG-CNC-90, FEG-CNC-110, FEG-CNC-130, FEG-CNC-150, FEG-CNC-180, and FEG-CNC-200, respectively.

Material Characterization: X-ray powder diffraction (XRD, Bruker D8) was performed in the 2θ range of 10°–80° to determine the crystalline phase and microcrystalline structures of the as-prepared CNCs. Raman spectra were acquired using the LabRAM3 HR800 spectrometer to gain insights into the carbon texture of the FEG-CNCs. To perform the in situ Raman tests, a 2025-type coin cell equipped with a hole in the top was used. After the coin battery was assembled, a thin glass slide was placed over the hole to seal it and prevent the electrolyte from being exposed to air. Raman data were collected during the charge–discharge test at a constant current of 0.3 mA covering the voltage range from 0.01 to 3 V. Fourier-transform infrared spectroscopy (FT–IR, Bruker, Germany) was used to collect the spectra of the materials. The surface chemical states of the elements in the samples were identified by X-ray photoelectron spectroscopy (XPS). The thermal stability and carbon contents of the samples were assessed by thermogravimetric analysis (TGA) using a Netzsch STA 449F3 analyzer within a temperature range from 30 to 1000 °C. The morphologies and microstructures of the EG-CNCs were investigated using scanning electron microscopy (SEM JIOL, JSM–7001F, 15 kV) and high-resolution transmission electron microscopy (HRTEM, JEOL, JEM2010, 15 kV). The N_2 adsorption/desorption tests were performed on a Micromeritics ASAP 2020 analyzer.

Electrochemical Measurement: The electrochemical performance of the electrode materials was investigated by assembling CR2025 coin cells in an argon-filled glove box (with O_2 < 0.1 ppm and H_2O < 0.1 ppm). The working electrodes were composed of FEG-CNCs (80 wt%), Super P carbon (10 wt%), and polyvinylidene fluoride (10 wt%). The three components were homogeneously dispersed in N–methyl–2–pyrrolidone (NMP) to form a slurry. The uniform slurry was coated on copper foil and dried at 120 °C in a vacuum oven for 12 h to prepare working electrodes. In the half cells, the potassium metal foil, glass fiber (Whatman), and 0.8 M KPF_6 (dissolved in ethylene carbonate (EC)/diethyl carbonate (DEC) (1:1 v/v)) were used as the counter electrode, the separator, and the electrolyte, respectively. A LAND CT 2001A test system was employed for conducting the galvanostatic charge–discharge (GCD) tests and the galvanostatic intermittent titration technique (GITT) measurements. Cyclic voltammetry (CV) curves and Electrochemical impedance spectra (EIS) were recorded on a CHI660E electrochemical workstation. The relevant molecular dynamics simulation parameters were shown in Supporting Information.

Supporting Information

Supporting Information is available from the Wiley Online Library or from the author.

Acknowledgements

The work was financially supported by the National Natural Science Foundation of China (52372213, 52172219, 22120102004, and U21A6004), Fundamental Research Program of Shanxi Province (202103021223019), Science and Technology Major Project of Shanxi (202101030201022), and the Priority Academic Program Development (PAPD) of Jiangsu Higher Education Institutions.

Conflict of Interest

The authors declare no conflict of interest.

Data Availability Statement

The data that support the findings of this study are available from the corresponding author upon reasonable request.

Keywords

carbon nanocages, energy storage, flash Joule heating, millisecond synthesis, potassium-ion batteries

Received: January 26, 2024
Revised: March 2, 2024
Published online: March 13, 2024

[1] D. Miranda, R. Gonçalves, S. Wuttke, C. M. Costa, S. Lanceros-Méndez, *Adv. Energy Mater.* **2023**, *13*, 2203874.
[2] G. J. Ji, J. X. Wang, Z. Liang, K. Jia, J. Ma, Z. F. Zhuang, G. M. Zhou, H. M. Cheng, *Nat. Commun.* **2023**, *14*, 584.
[3] H. E. Melin, M. A. Rajaeifar, A. Y. Ku, A. Kendall, G. Harper, O. Heidrich, *Science* **2021**, *373*, 384.
[4] J. S. Zhang, Y. C. Wang, M. H. Yu, J. F. Ni, L. Li, *ACS Energy Lett.* **2022**, *7*, 1835.
[5] Y. N. Chen, Y. J. Li, Y. B. Wang, K. Fu, V. A. Danner, J. Q. Dai, S. D. Lacey, Y. G. Yao, L. B. Hu, *Nano Lett.* **2016**, *16*, 5553.
[6] J. W. Luo, J. C. Zhang, Z. X. Guo, Z. D. Liu, S. M. Dou, W. D. Liu, Y. N. Chen, W. B. Hu, *Nano Res.* **2023**, *16*, 4240.
[7] D. W. Zhang, X. M. Ma, L. C. Wu, J. Wen, F. X. Li, J. Zhou, A. M. Rao, B. G. Lu, *Adv. Energy Mater.* **2023**, *13*, 2203277.
[8] Y. H. Feng, A. M. Rao, J. Zhou, B. G. Lu, *Adv. Mater.* **2023**, *35*, 2300886.
[9] K. Sada, J. Darga, A. Manthiram, *Adv. Energy Mater.* **2023**, *13*, 2302321.
[10] K. C. Wang, S. H. Liu, J. T. Zhang, Z. W. Hu, Q. Y. Kong, Y. Xu, X. Q. Huang, *ACS Nano* **2022**, *16*, 15008.
[11] Z. H. Sun, Y. Liu, W. B. Ye, J. Y. Zhang, Y. Y. Wang, Y. Lin, L. R. Hou, M. S. Wang, C. Z. Yuan, *Angew. Chem., Int. Ed.* **2021**, *60*, 7180.
[12] Y. H. Sun, D. M. Zhu, Z. F. Liang, Y. X. Zhao, W. F. Tian, X. C. Ren, J. Wang, X. Y. Li, Y. Gao, W. Wen, Y. B. Huang, X. L. Li, R. Z. Tai, *Carbon* **2020**, *167*, 685.
[13] B. Cao, Q. Zhang, H. Liu, B. Xu, S. L. Zhang, T. F. Zhou, J. F. Mao, W. K. Pang, Z. P. Guo, A. Li, J. S. Zhou, X. H. Chen, H. H. Song, *Adv. Energy Mater.* **2018**, *8*, 1801149.
[14] C. J. Thambiliyagodage, S. Ulrich, P. T. Araujo, M. G. Bakker, *Carbon* **2018**, *134*, 452.
[15] H. C. Xia, K. X. Li, Y. Y. Guo, J. H. Guo, Q. Xu, J. N. Zhang, *J. Mater. Chem. A* **2018**, *6*, 7148.
[16] W. L. Zhang, J. Ming, W. L. Zhao, X. C. Dong, M. N. Hedhili, P. M. F. J. Costa, H. N. Alshareef, *Adv. Funct. Mater.* **2019**, *29*, 1903641.
[17] R. D. Hunter, J. Ramírez-Rico, Z. Schnepp, *J. Mater. Chem. A* **2022**, *10*, 4489.
[18] Q. G. Wang, C. L. Li, L. He, X. F. Yu, W. P. Zhang, A. H. Lu, *J. Colloid Interf. Sci.* **2021**, *599*, 586.
[19] Y. N. Chen, G. C. Egan, J. Y. Wan, S. Z. Zhu, R. J. Jacob, W. B. Zhou, J. Q. Dai, Y. B. Wang, V. A. Danner, Y. G. Yao, K. Fu, Y. B. Wang, W. Z. Bao, T. Li, M. R. Zachariah, L. B. Hu, *Nat. Commun.* **2016**, *7*, 12332.
[20] M. A. S. R. Saadi, P. A. Advincula, M. S. H. Thakur, A. Z. Khater, S. Saad, A. S. Zeraati, S. K. Nabil, A. Zinke, S. Roy, M. Lou, S. Bheemasetti, M. A. A. Bari, Y. W. Zheng, J. L. Beckham, V. Gadhamshetty, A. Vashisth, M. G. Kibria, J. M. Tour, P. M. Ajayan, M. M. Rahma, *Sci. Adv.* **2022**, *8*, eadd3555.
[21] Y. Li, C. Zhou, X. J. Xie, G. Q. Shi, L. T. Qu, *Carbon* **2010**, *48*, 4190.
[22] D. X. Luong, K. V. Bets, W. A. Algozeeb, M. G. Stanford, C. Kittrell, W. Y. Chen, R. V. Salvatierra, M. Q. Ren, E. A. McHugh, P. A. Advincula, Z. Wang, M. Bhatt, H. Guo, V. Mancevski, R. Shahsavari, B. I. Yakobson, J. M. Tour, *Nature* **2020**, *577*, 647.
[23] K. M. Wyss, D. X. Luong, J. M. Tour, *Adv. Mater.* **2022**, *34*, 2106970.
[24] S. Zhu, F. Zhang, H. G. Lu, J. Sheng, L. N. Wang, S. D. Li, G. Y. Han, Y. Li, *ACS Mater. Lett.* **2022**, *4*, 1863.
[25] W. Y. Chen, J. T. Li, C. Ge, Z. Yuan, W. A. Algozeeb, P. A. Advincula, G. H. Gao, J. H. Chen, K. X. Ling, C. H. Choi, E. A. McHugh, K. M. Wyss, D. X. Luong, Z. Wang, Y. M. Han, J. M. Tour, *Adv. Mater.* **2022**, *34*, 2202666.
[26] R. Q. Tian, L. P. Duan, Y. F. Xu, Y. H. Man, J. L. Sun, J. C. Bao, X. S. Zhou, *Energy Environ. Mater.* **2023**, *6*, e12617.
[27] S. H. Choi, J. Baucom, X. Li, L. Shen, Y. H. Seong, I. S. Han, Y. J. Choi, Y. N. Ko, H. J. Kim, Y. F. Lu, *J. Colloid Interf. Sci.* **2020**, *577*, 48.
[28] J. F. Ni, X. C. Zhu, Y. F. Yuan, Z. Z. Wang, Y. B. Li, L. Ma, A. Dai, M. Li, T. P. Wu, R. Shahbazian-Yassar, J. Lu, L. Li, *Nat. Commun.* **2020**, *11*, 1212.
[29] W. C. Feng, C. Q. Pan, H. Wang, B. L. Zhang, W. Luo, C. L. Shen, J. J. Wang, C. J. Cheng, X. M. Xv, R. H. Yu, Y. B. Guo, L. Q. Mai, *Energy Storage Mater.* **2023**, *63*,102975.
[30] J. Wang, Z. Xu, J. C. Eloi, M. M. Titirici, S. J. Eichhorn, *Adv. Funct. Mater.* **2022**, *32*, 2110862.
[31] J. Sheng, Z. Han, G. D. Jia, S. Zhu, Y. F. Xu, X. R. Zhang, Y. X. Yao, Y. Li, *Adv. Funct. Mater.* **2023**, *33*, 2306785.
[32] W. Huang, Z. H. Ma, L. Zhong, K. T. Luo, W. Li, S. K. Zhong, D. L. Yan, *Small* **2023**, *20*, 2304690.
[33] Y. S. Wang, Z. P. Wang, Y. J. Chen, H. Zhang, M. Yousaf, H. S. Wu, M. C. Zou, A. Y. Cao, R. P. S. Han, *Adv. Mater.* **2018**, *30*, 1802074.
[34] J. X. Hu, Y. Y. Xie, M. Yin, Z. A. Zhang, *J. Energy Chem.* **2020**, *49*, 327.
[35] N. Yang, R. Shao, Z. P. Zhang, M. L. Dou, J. Niu, F. Wang, *Carbon* **2021**, *178*, 775.
[36] K. Y. Zou, Z. R. Song, X. Gao, H. Q. Liu, Z. Luo, J. Chen, X. L. Deng, L. B. Chen, G. Q. Zou, H. S. Hou, X. B. Ji, *Angew. Chem., Int. Ed.* **2021**, *60*, 17070.
[37] Y. Lei, D. Han, J. H. Dong, L. Qin, X. J. Li, D. Y. Zhai, B. H. Li, Y. Y. Wu, F. Y. Kang, *Energy Storage Mater.* **2020**, *24*, 319.
[38] Z. Y. Wang, K. Z. Dong, D. Wang, S. H. Luo, Y. G. Liu, Q. Wang, Y. H. Zhang, A. M. Hao, C. S. Shi, N. Q. Zhao, *J. Mater. Chem. A* **2019**, *7*, 14309.
[39] Y. H. Feng, Y. W. Lv, H. W. Fu, M. Parekh, A. M. Rao, H. Wang, X. L. Tai, X. H. Yi, Y. Lin, J. Zhou, B. G. Lu, *Natl Sci Rev* **2023**, *10*, nwad118.
[40] B. Wang, Z. Y. Zhang, F. Yuan, D. Zhang, Q. J. Wang, W. Li, Z. J. Li, Y. M. A. Wu, W. Wang, *Chem. Eng. J.* **2022**, *428*, 131093.

[41] X. M. Ma, H. W. Fu, J. Y. Shen, D. W. Zhang, J. W. Zhou, C. Y. Tong, A. M. Rao, J. Zhou, L. Fan, B. G. Lu, *Angew. Chem., Int. Ed.* **2023**, *62*, e202312973.
[42] X. H. Yi, A. M. Rao, J. Zhou, B. G. Lu, *Nano-Micro Lett.* **2023**, *15*, 200.
[43] M. T. Xia, H. W. Fu, K. R. Lin, A. M. Rao, L. M. Cha, H. Liu, J. Zhou, C. X. Wang, B. G. Lu, *Energy Environ. Sci.* **2024**, *17*, 1255.
[44] X. Qiu, L. L. Shi, Z. H. Xu, J. J. Qian, M. Song, L. M. Sun, X. N. Xu, Y. Xu, Y. Z. Fu, J. Z. Ren, W. C. Zhuang, Q. C. Zhuang, Z. C. Ju, Y. X. Chen, *J. Alloy. Compd.* **2024**, *970*, 172539.
[45] A. M. A. Mohamed, S. Dong, M. Elhefnawey, G. S. Dong, Y. Y. Gao, K. Zhu, D. X. Cao, *Chem. Phys. Lett.* **2023**, *815*,140362.
[46] X. Q. Chang, N. Sun, H. Y. Zhou, R. A. Soomro, B. Xu, *Chinese Chem. Lett.* **2023**, *34*, 107312.
[47] Z. M. Liu, J. Wang, X. X. Jia, W. L. Li, Q. F. Zhang, L. Fan, H. B. Ding, H. G. Yang, X. Z. Yu, X. K. Li, B. G. Lu, *ACS Nano* **2019**, *13*,10631.
[48] Y. Liu, Y. X. Lu, Y. S. Xu, Q. S. Meng, J. C. Gao, Y. G. Sun, Y. S. Hu, B. B. Chang, C. T. Liu, A. M. Cao, *Adv. Mater.* **2020**, *32*, 2000505.
[49] W. Tan, L. N. Wang, K. Liu, Z. G. Lu, F. Yang, G. F. Luo, Z. H. Xu, *Small* **2022**, *18*, 2203494.
[50] C. Y. Meng, M. Yuan, B. Cao, X. J. Lin, J. P. Zhang, A. Li, X. H. Chen, M. Q. Jia, H. H. Song, *Carbon* **2022**, *192*, 347.
[51] W. Wang, J. H. Zhou, Z. P. Wang, L. Y. Zhao, P. H. Li, Y. Yang, C. Yang, H. X. Huang, S. J. Guo, *Adv. Energy Mater.* **2018**, *8*, 1701648.
[52] Y. Z. Zhang, X. J. Chen, W. L. Cen, W. H. Ren, H. C. Guo, S. C. Wu, Y. Xiao, S. Chen, Y. Guo, D. Xiao, C. Zhao, *Nano Res.* **2022**, *15*, 4083.
[53] L. F. Yang, Y. Q. Zhu, X. Y. Yao, C. L. Du, Z. N. Han, J. C. Tian, X. Liu, X. L. Ma, C. B. Cao, *Energy Storage Mater.* **2023**, *63*, 102972.
[54] X. D. Li, J. L. Li, L. Ma, C. Y. Yu, Z. Ji, L. K. Pan, W. J. Mai, *Energy Environ. Mater.* **2022**, *5*, 458.
[55] Y. L. An, H. F. Fei, G. F. Zeng, L. J. Ci, B. J. Xi, S. L. Xiong, J. K. Feng, *J. Power Sources* **2018**, *378*, 66.
[56] L. Fan, R. F. Ma, Q. F. Zhang, X. X. Jia, B. G. Lu, *Angew. Chem., Int. Ed.* **2019**, *58*, 10500.
[57] J. L. Liu, T. T. Yin, B. B. Tian, B. W. Zhang, C. Qian, Z. Q. Wang, L. L. Zhang, P. Liang, Z. Chen, J. X. Yan, X. F. Fan, J. Y. Lin, X. H. Chen, Y. Z. Huang, K. P. Loh, Z. X. Shen, *Adv. Energy Mater.* **2019**, *9*, 1900579.
[58] S. F. Zeng, X. F. Zhou, B. Wang, Y. Z. Feng, R. Xu, H. B. Zhang, S. M. Peng, Y. Yu, *J. Mater. Chem. A* **2019**, *7*, 15774.
[59] L. J. Xu, Z. Gong, C. Y. Zhang, N. Li, Z. M. Tang, J. J. Du, *J. Alloy. Compd* **2023**, *934*, 167820.
[60] G. B. Chen, R. H. Lu, C. Z. Li, J. M. Yu, X. D. Li, L. M. Ni, Q. Zhang, G. Q. Zhu, S. W. Liu, J. X. Zhang, U. I. Kramm, Y. Zhao, G. Wu, J. Xie, X. L. Feng, *Adv. Mater.* **2023**, *35*, 2300907.
[61] Z. U. Ahmad, B. Chao, M. I. Konggidinata, Q. Lian, M. E. Zappi, D. D. Gang, *J. Hazard. Mater.* **2018**, *354*, 258.
[62] C. C. Liu, Q. Q. Lu, M. V. Gorbunov, A. Omar, I. G. G. Martinez, P. P. Zhao, M. Hantusch, A. D. C. Permana, H. Y. He, N. Gaponik, D. Mikhailova, *J. Energy Chem.* **2023**, *79*, 373.
[63] J. Feng, S. H. Luo, Y. C. Lin, Y. Zhan, S. X. Yan, P. Q. Hou, Q. Wang, Y. H. Zhang, *J. Power Sources* **2022**, *535*, 231444.
[64] Y. Yang, Y. Ma, X. J. Wang, Z. C. Gao, J. G. Yu, T. Liu, *Chem. Eng. J.* **2023**, *455*, 140610.
[65] Y. Y. He, L. Wang, C. F. Dong, C. C. Li, X. Y. Ding, Y. T. Qian, L. Q. Xu, *Energy Storage Mater.* **2019**, *23*, 35.
[66] Q. P. Li, R. S. Deng, Y. X. Chen, J. Gong, P. Wang, Q. J. Zheng, Y. Huo, F. Y. Xie, X. J. Wei, C. H. Yang, D. M. Lin, *Small* **2023**, *19*, 2303642.
[67] H. Y. Yang, L. J. Sun, S. L. Zhai, X. Wang, C. C. Liu, H. Wu, W. Q. Deng, *ACS Appl. Nano Mater* **2023**, *6*, 2450.
[68] J. H. Chu, C. J. Zhang, X. W. Wu, L. D. Xing, J. G. Zhang, L. Q. Zhang, H. C. Wang, W. Wang, Q. Y. Yu, *Small* **2023**, *19*, 2304406.
[69] S. W. Sun, X. N. Li, L. Q. Yan, W. X. Chen, X. Lu, Y. Bai, *ACS Energy Lett.* **2023**, *8*, 4349.
[70] S. Zhu, L. N. Wang, C. Y. Gu, H. C. Liu, Y. W. Mu, J. F. Ni, G. Y. Han, *J. Power Sources* **2022**, *532*, 231335.
[71] Z. Y. Huang, Y. F. Yuan, Z. J. Yao, M. Zhu, S. M. Yin, Y. Z. Huang, S. Y. Guo, W. W. Yan, *Appl. Surf. Sci.* **2023**, *637*, 157886.
[72] H. N. Wang, K. F. Yu, P. T. Wang, P. C. Jia, Y. Z. Yuan, C. Liang, *J. Colloid Interf. Sci.* **2023**, *645*, 55.
[73] S. Zhu, Y. Z. Chang, W. J. Hou, Y. P. Li, J. F. Ni, G. Y. Han, *Carbon* **2022**, *200*, 75.
[74] X. Sun, Z. J. Li, Z. X. Liu, X. W. Lv, K. Q. Shi, R. J. Chen, F. Wu, L. Li, *Adv. Funct. Mater.* **2023**, *33*, 2300125.
[75] Y. Zhao, Y. Li, C. L. Ma, Z. P. Shao, *Electrochim. Acta* **2016**, *213*, 98.